J. Fluid Mech. (1985), *vol.* 160, *pp.* 181–210
Printed in Great Britain

Countercurrent convection in a double-diffusive boundary layer

By R. H. NILSON
S-Cubed, P.O. Box 1620, La Jolla, CA 92038

(Received 4 April 1984 and in revised form 15 May 1985)

Countercurrent flow may be induced by opposing buoyancy forces associated with compositional gradients and thermal gradients within a fluid. The occurrence and structure of such flows is investigated by solving the double-diffusive boundary-layer equations for steady laminar convection along a vertical wall of finite height. Non-similar solutions are derived using the method of matched asymptotic expansions, under the restriction that the Lewis and Prandtl numbers are both large. Two sets of asymptotic solutions are constructed, assuming dominance of one or the other of the buoyancy forces. The two sets overlap in the central region of the parameter space; each set matches up with neighbouring unidirectional similarity solutions at the respective borderlines of incipient counterflow.

Interaction between the buoyancy mechanisms is controlled by their relative strength R and their relative diffusivity Le. Flow in the outer thermal boundary layer deviates from single-diffusive thermal convection, depending upon the magnitude of the parameter RLe. Flow in the inner compositional boundary layer deviates from single-diffusive compositional convection, depending upon the magnitude of $RLe^{\frac{1}{3}}$.

1. Introduction

In double-diffusive natural convection the driving density gradients result from gradients of two components having different molecular diffusivities (Turner 1974). Both components might be dissolved substances, such as salt and sugar. More often, one component is heat and the other is a solute. In either instance the physical mechanisms and the governing equations are essentially the same. So, without loss of generality, the present discussion will address the thermosolutal case, in which one gradient is thermal and the other is compositional.

Double-diffusive convection provides an explanation for a number of natural phenomena (Huppert & Turner 1981) such as thermohaline layering of the ocean, seawater intrusion into freshwater lakes, and the formation of layered or columnar structures during crystallization of igneous intrusions in the Earth's crust. In addition, there are a number of current engineering applications (Chen & Johnson 1984) in which double diffusion is important, such as energy storage in solar ponds, rollover in storage tanks containing liquified natural gas, solution mining of salt caverns for crude oil storage, and casting of metal alloys.

The character of a double-diffusive convective motion depends upon the orientation of the two density gradients with respect to the gravitational field (Turner 1974). Three different cases can be distinguished. If both gradients are vertical the configuration resembles the Rayleigh–Bénard stability problem, except that double-diffusive instabilities can develop even when the net density decreases upwards and the system would appear to be statically stable. Alternatively, if one density gradient,

say compositional, is vertical and statically stable the imposition of a horizontal temperature gradient at a vertical or inclined boundary will induce a multicellular intrusive motion along the boundary. Finally, both of the density gradients might be horizontal, resulting in a boundary-layer flow along a vertical or inclined boundary. This last case is the subject of the present study.

Previous analyses of double-diffusive boundary layers have generally been based upon a self-similar formulation, and the resulting ordinary differential equations have been solved by analytical approximations or by numerical methods (Ostrach 1980; Wilcox 1961; Saville & Churchill 1970; Adams & McFadden 1966; Gebhart & Pera 1971; Chen & Yuh 1979; Carey & Gebhart 1982*a*,*b*; Nilson & Baer 1982). When the two buoyancy forces aid one another the fluid moves primarily in one direction, as in single-diffusive convection, and there is no difficulty in making accurate predictions. However, when the buoyancy forces oppose one another the flow structure may be far more complex, because opposite motions can occur within different regions of the boundary layer. Gebhart & Pera (1971) were the first to demonstrate the existence of countercurrent, or backflow, solutions to the self-similar equations. But the flow reversals they reported were very weak, and they pointed out that numerical difficulties were encountered in computing even these marginal cases of flow reversal, as reaffirmed by Carey & Gebhart (1982*a*,*b*). A probable explanation for their numerical difficulty is the existence of multiple solutions in the neighbourhood of incipient counterflow.

The occurrence of counterflow *vs.* unidirectional flow in a double-diffusive boundary layer depends upon the relative strength of the two buoyancy forces and on the relative diffusivity of the two buoyant components. The borderlines between the unidirectional and counterflow regimes have been mapped out (Nilson & Baer 1982) on the basis of self-similar analysis, by systematically sweeping through the parameter space and recording the parameter values whenever incipient counterflow was encountered. In the course of this exercise a loop-like multiplicity of solutions was found to always occur in the near neighbourhood of incipient counterflow, somewhat in analogy with the Falkner–Skan counterflows (Veldman 1980). Although the self-similar counterflows were confirmed to occur, it became apparent that, within the self-similar context, the backflow region can only be very weak and that there is a large region of the parameter space in which self-similar solutions are inadmissible. Shortly thereafter, the non-existence of similarity solutions was rigorously proved by Romero (1982) for a particular case in which the buoyancy forces were in close balance. The non-existence of similarity solutions does not imply a radical transition in the physical phenomena – but only that a more general class of mathematical functions is required to describe the motion.

Experiments by Carey & Gebhart (1982*b*) and by Sammakia & Gebhart (1983) confirm the existence of laminar bidirectional flows along vertical ice surfaces melting in salt water. Although these experiments are influenced by the density extremum of water near its melting point (Carey & Gebhart 1981), the primary cause of the bidirectional motion is often the double diffusion of heat and salt; this is particularly true when the salinity of the water is high. Comparisons between experiments and calculations by Carey & Gebhart (1982*a*,*b*) verify that the borderlines of incipient counterflow are properly predicted by self-similar boundary-layer theory. They point out, however, that a less restrictive analysis is required to predict the bidirectional transport problem.

A particular motivation for the present study is the possible occurrence of double-diffusive boundary-layer convection in kilometre-scale chambers of molten

rock known to exist at relatively shallow depths within the Earth's crust. Although the relatively cold wall of the chamber would generally induce a descending boundary layer, an opposing upward buoyancy is associated with the compositional gradients resulting from the hydration (Shaw 1974) or the crystal fractionation (McBirney 1980), which occur respectively during melting or freezing at the wall. Laboratory simulations by Chen & Turner (1980), McBirney (1980) and Turner (1980) have illustrated the occurrence of bidirectional boundary-layer flows under these circumstances, with compositionally altered fluid flowing up the wall to collect in a stratified cap at the top of the chamber (Walin 1971). The formation of such a stratified layer provides a plausible explanation for observed volcanic-eruption sequences (McBirney 1980), a water-rich cap could lead to explosive volcanism owing to vapour formation during pressure release, and such a stratification could result in the double-diffusive layering motions thought to explain layered igneous intrusions like Skaergaard (McBirney & Noyes 1979).

The present study explores the counterflow regime of double-diffusive boundary-layer convection. The analysis is based upon the method of matched asymptotic expansions, under the restriction that the Prandtl and Lewis numbers must both be large. This restriction is marginally satisfied in the applications dealing with heat and mass transfer in aqueous solutions; it is very strongly satisfied in the geological applications dealing with molten rock. The asymptotic matching procedure is first tested within the context of double-diffusive flows that are unidirectional and hence self-similar. In applying the method to non-similar bidirectional flows the resulting partial differential equations are solved by a local non-similar expansion procedure. This approach circumvents the difficulties normally associated with integrating the boundary-layer equations through a region of reversed flow (Klemp & Acrivos 1972; Cebeci & Stewartson 1983).

2. Governing equations

The boundary-layer equations describe the transport of mass, momentum, energy and chemical species for a binary fluid/solute flow along a vertical wall (Gebhart & Pera 1971):

$$\frac{\partial u}{\partial x}+\frac{\partial v}{\partial y}=0, \tag{1}$$

$$u\frac{\partial u}{\partial x}+v\frac{\partial u}{\partial y}=\nu\frac{\partial^2 u}{\partial y^2}+g\beta_{\mathrm{t}}(\theta-\theta_\infty)+g\beta_{\mathrm{c}}(\phi-\phi_\infty), \tag{2}$$

$$u\frac{\partial \theta}{\partial x}+v\frac{\partial \theta}{\partial y}=\kappa\frac{\partial^2 \theta}{\partial y^2}, \tag{3}$$

$$u\frac{\partial \phi}{\partial x}+v\frac{\partial \phi}{\partial y}=D\frac{\partial^2 \phi}{\partial y^2}. \tag{4}$$

Here x and y measure distance along the wall and normal to the wall, respectively; u and v are the corresponding components of velocity; while θ and ϕ denote temperature and solute concentration. Fluid properties are presumed constant, except in the Boussinesq treatment of density variations resulting from thermal expansion (coefficient β_{t}) and from solutal concentration (coefficient β_{c}).

Consider the fundamental case in which the wall is impermeable and the temperature and concentration are each uniform along the wall ($y = 0$) and in the far field ($y \to \infty$).

By introduction of dimensionless variables

$$T = \frac{\theta - \theta_\infty}{\theta_0 - \theta_\infty}, \quad C = \frac{\phi - \phi_\infty}{\phi_0 - \phi_\infty} \tag{5}$$

the boundary conditions can be written as

$$T(x,0) = C(x,0) = 1, \quad u(x,0) = v(x,0) = 0, \tag{6}$$

$$T(x,\infty) = C(x,\infty) = 0, \quad u(x,\infty) = 0. \tag{7}$$

In taking $v(x,0) = 0$ we suppress any mass flux across the wall, as might occur in a dissolution or melting process. Under this rather mild restriction the roles of T and C are entirely interchangeable.

Three different diffusivities appear in the transport equations: chemical diffusivity D, thermal diffusivity κ and momentum diffusivity ν. Because of this there are three different transverse lengthscales or boundary-layer thicknesses: compositional thickness δ_c, thermal thickness δ_t and viscous thickness δ_ν. The ordering is

$$\delta_\nu \gg \delta_t \gg \delta_c \tag{8}$$

in the case considered, where

$$\nu \gg \kappa \gg D, \tag{9}$$

or equivalently

$$Pr = \frac{\nu}{\kappa} \gg 1, \quad Le = \frac{\kappa}{D} \gg 1, \tag{10}$$

in which Pr and Le are the Prandtl and Lewis numbers.

For clarity of discussion, let us suppose that the compositional buoyancy tends to induce an upward motion near the wall and that the thermal buoyancy tends to induce a downward motion in the far field. There is no loss of generality in adopting these conventions; it is only important that the buoyancy forces act in opposite directions and that there be a disparity of diffusivity. Thus the analysis is applicable either to small Lewis number or large Lewis number, since the roles of T and C are interchangeable.

The interaction between the two buoyancy mechanisms depends mainly on the relative strength R of the buoyancy forces,

$$R = \frac{|\beta_t \Delta\theta|}{|\beta_c \Delta\phi|} = \frac{|\Delta\rho_t|}{|\Delta\rho_c|} > 0, \tag{11}$$

and on the relative diffusivity $Le = \kappa/D$ of the two components. As indicated schematically in the flow-regime map of figure 1, three different situations are possible (Nilson & Baer 1982):

(i) unidirectional downflow occurs when $R \lesssim 1/Le^{\frac{1}{3}}$;
(ii) unidirectional upflow occurs when $R \lesssim 1/Le$;
(iii) bidirectional counterflow occurs when $1/Le^{\frac{1}{3}} \lesssim R \lesssim 1/Le$.

The nature of the motion depends upon which of the components is dominant. If the more-diffusive component (heat) is dominant let us refer to the situation as *outer-dominated*. If the less-diffusive component (solute) is dominant let us attach the label *inner dominated*. A somewhat arbitrary division between these two regimes is the line $R = 1/Le^{\frac{1}{3}}$ which cuts through the centre of the counterflow regime. This inner- *vs.* outer-dominated distinction is useful only in describing the mathematical

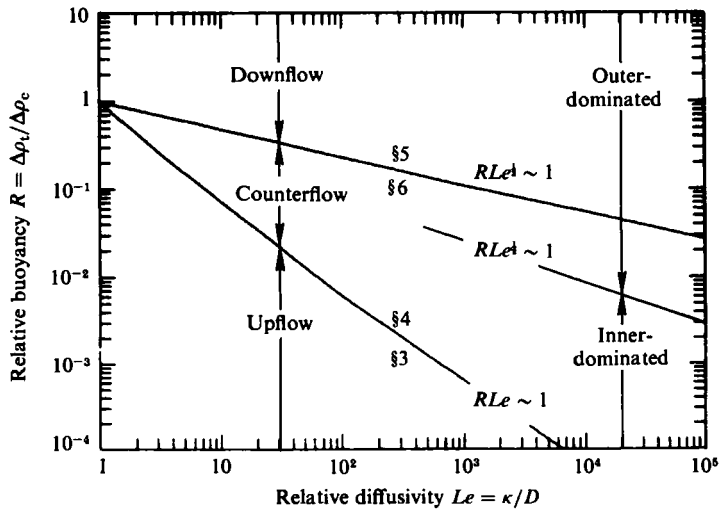

FIGURE 1. Flow-regime map showing regions of upflow, downflow and counterflow. Upward motion is induced by less-diffusive (inner) compositional buoyancy mechanism. Downward motion is induced by more-diffusive (outer) thermal buoyancy mechanisms. Numbers refer to sections of the paper in which various regimes are discussed.

approach used to solve the problem, since there is obviously a broad central region in which neither force is clearly dominant.

The course of our discussion is charted in figure 1, where section numbers of the paper are identified with corresponding regions of the parameter space. We begin in §3 by solving the self-similar problem of unidirectional upflow; this serves mainly as a test of the asymptotic matching technique which is used throughout the paper. In §4 that same technique is applied to non-similar counterflows which are dominated by the inner, or less-diffusive, buoyancy mechanism. Sections 5 and 6 respectively address the unidirectional and countercurrent flows which are dominated by the outer, or more-diffusive, buoyancy mechanism. Finally, in §7 it is shown that, within the central part of the counterflow regime, the inner-dominated solutions of §4 are almost identical with the outer-dominated solutions of §6.

3. Inner-dominated similarity solutions

The less-diffusive component, here solute, is dominant for sufficiently small values of the buoyancy ratio R. In the limit as R tends to zero the thermal buoyancy is entirely absent, and the motion must be identical with single-diffusive convection driven by solutal buoyancy alone. That problem has been previously analysed by Kuiken (1968) using the method of matched asymptotic expansions. So here we will use Kuiken's scaling and his matching arguments as a starting point for our treatment of the double-diffusive problem.

The partial differential equations (1)–(3) are reduced to ordinary differential equations by the introduction of a similarily variable η and a normalized stream function f (Kuiken 1968):

$$\eta = \frac{cy}{x^{\frac{1}{4}}} Sc^{\frac{1}{4}}, \quad f = \frac{\psi}{4\nu c x^{\frac{3}{4}}} Sc^{\frac{3}{4}}. \tag{12}$$

Here ψ is the stream function, $c = (g\beta_c \Delta\phi/4\nu^2)^{\frac{1}{4}}$, and x is measured in the primary direction of flow, which is taken as upward for the inner-dominated case. Under the

stated similarity transformation the equations take the following form, in which primes denote derivatives with respect to η:

$$f''' + C - RT = \frac{2f'^2 - 3ff''}{Sc}, \tag{13}$$

$$C'' + 3fC' = 0, \tag{14}$$

$$T'' + \frac{3fT'}{Le} = 0, \tag{15}$$

subject to the boundary conditions

$$f(0) = f'(0) = 0, \quad C(0) = T(0) = 1, \tag{16}$$

$$f'(\infty) = 0, \quad C(\infty) = T(\infty) = 0. \tag{17}$$

The key parameters are the buoyancy ratio R and the diffusivity ratio Le. The Schmidt number Sc also appears above, but it can be eliminated as explained in the next paragraph.

The inertial terms can be deleted from the momentum equation (13) as Sc tends to infinity, but the equations must then be restricted to the buoyant layer(s) close to the wall, where the shear forces are in balance with buoyancy forces. At the outer edge of this buoyant zone the buoyancy force becomes small, and so must the shear. Hence the boundary condition

$$f''(\infty) = 0 \tag{18}$$

replaces the more familiar condition of vanishing velocity, $f'(\infty) = 0$, as rigorously justified by Kuiken (1968). Of course, the velocity does fall back to zero, but only on the much broader lengthscale of the viscous boundary layer, in which shear forces are balanced by inertial forces, and buoyancy forces are absent.

Numerical solutions of the double-diffusive boundary-layer equations (13)–(18) are presented in figures 2 and 3 for $Le = 100$ and $Sc \to \infty$. The computations were done using a numerical implementation of Picards's method, as described by Nilson & Baer (1982). The parameter that varies in the plots is the product $R\,Le$ which obviously increases as R increases. When $R = 0$ thermal buoyancy is fully suppressed and the velocity rises monotonically to a maximum of $f'(\infty) = 0.51$, in agreement with Kuiken's (1968) single-diffusive analysis. For non-zero values of R the velocity rises to a local maximum at the outer edge of the compositional layer where $\eta \sim 1$. But further from the wall the opposing thermal buoyancy reduces the upward velocity. For $R\,Le = 0.62$ the thermal buoyancy is nearly strong enough to cause a slight flow reversal at the outer edge of the buoyant region. However, the more significant flow reversal that occurs at even larger $R\,Le$ is not compatible with the assumed self-similar form of the solution.

A negative velocity at the outer edge of the buoyant region would imply that the stream function must eventually become negative at some distance from the wall. Within the self-similar context this would imply that the temperature and concentration increase exponentially, rather than decrease as they must in order to satisfy the boundary conditions. A more complete explanation of this mathematical difficulty is given by Nilson & Baer (1982), and Romero (1982) presents a formal proof that inner-dominated similarity solutions cannot exist for $R\,Le$ near unity. Thus it will be necessary to consider non-similar flow structures, as discussed in §4. These non-similar solutions will require matching of an upward-flowing compositional layer

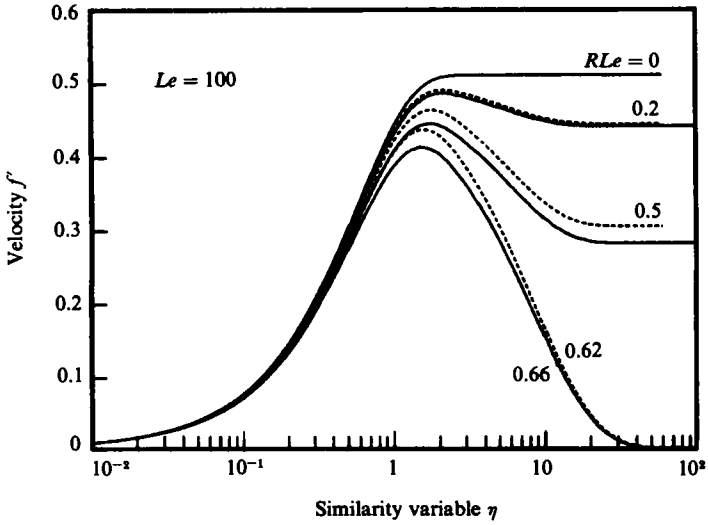

FIGURE 2. Self-similar velocity profiles for inner-dominated flow with varying strength RLe of opposing buoyancy force: comparison of matched asymptotic expansions (——) with exact numerical results (· · · · ·). Incipient counterflow occurs at $RLe = 0.62$ and 0.66 respectively for exact and asymptotic solutions.

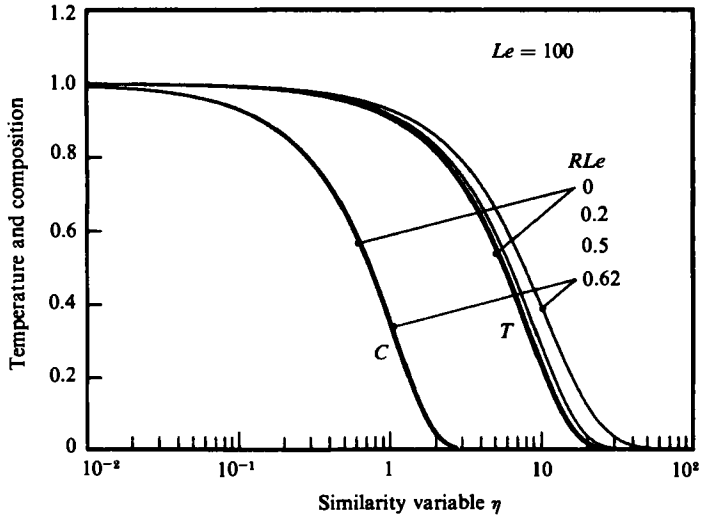

FIGURE 3. Self-similar composition and temperature profiles for inner-dominated flow: exact numerical solutions for various strengths of opposing buoyancy force. Thermal layer is much broader than compositional layer.

with a downward-flowing thermal layer. As a prelude to these non-similar applications, let us first apply the same matching technique to the self-similar flows of figure 2. This cross-checking of similarity solutions will afford greater confidence in the subsequent-non-similar applications, for which no comparative solutions exist.

At high Lewis number the compositional boundary layer is much thinner than the thermal boundary layer, as illustrated by the composition and temperature profiles

in figure 3. In the limit of large Le, with $R\,Le$ held fixed, the inner compositional layer can be described by a reduced system of equations

$$f''' + C = 0, \tag{19}$$

$$C'' + 3fC' = 0, \tag{20}$$

$$T = 1, \tag{21}$$

with boundary conditions

$$f(0) = f'(0) = 0, \quad C(0) = 1, \tag{22}$$

$$f''(\infty) = 0, \quad C(\infty) = 0. \tag{23}$$

Within this innermost layer the temperature is essentially uniform, and the thermal buoyancy can be safely neglected for the inner-dominated conditions of interest, as for example in figure 2 where $R < 0.01$. The thermal buoyancy effects will, of course, be later included in the outer equations. The physical motivation for the no-shear boundary condition, $f'' = 0$, is apparent in the computed velocity profiles of figure 2, and it will be verified through the matching formalism.

The outer thermal boundary layer can be described by a slightly different scaling of the similarity variables:

$$\eta^* = \frac{c^* y}{x^{\frac{1}{4}}} Pr^{\frac{1}{4}}, \quad f^* = \frac{\psi}{4\nu c^* x^{\frac{3}{4}}} Pr^{\frac{3}{4}}. \tag{24}$$

This is precisely the scaling that would be appropriate for a single-diffusive flow driven by thermal buoyancy alone. In analogy with the inner scaling in (12), Pr now replaces Sc and the thermal buoyancy $\Delta\rho_t$ replaces the compositional buoyancy in defining the scaling constant $c^* = (g\beta_t \Delta\theta/4\nu^2)^{\frac{1}{4}}$. However, very importantly, x is the same as before; it increases in the upward direction. Under this transformation, the thermal boundary-layer equations can be written in the following form, where primes represent derivatives with respect to η^*:

$$f^{*'''} - T = 0, \tag{25}$$

$$T'' + 3f^*T' = 0, \tag{26}$$

$$C = 0, \tag{27}$$

subject to the inner/outer matching conditions (verified in next paragraph)

$$f^*(0) = 0; \quad T(0) = 1, \tag{28}$$

$$\frac{\mathrm{d}f^*}{\mathrm{d}\eta^*}(0) = \frac{\mathrm{d}f}{\mathrm{d}\eta}(\infty)\frac{1}{(R\,Le)^{\frac{1}{2}}} = \frac{0.51}{(R\,Le)^{\frac{1}{2}}}, \tag{29}$$

as well as the far-field boundary conditions

$$f^{*\prime}(\infty) = 0, \quad T(\infty) = 0. \tag{30}$$

The no-shear condition is appropriate at the outer edge because the thermal layer is much thinner than the viscous layer whenever Pr is large.

The matching conditions between the inner and outer buoyancy layers can be verified by writing the outer expansion of the inner solution as

$$\lim_{\eta\to\infty} f = a_0 + a_1\eta + a_2\eta^2 + \text{exponentially small terms} \tag{31}$$

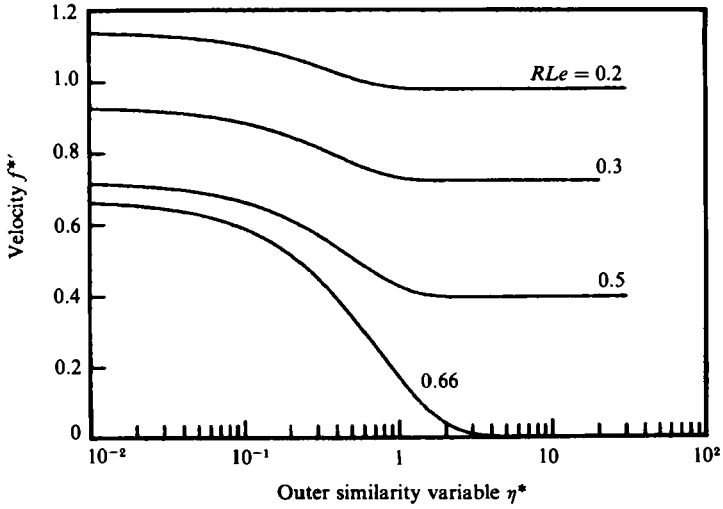

FIGURE 4. Velocity decreases in moving outward across the thermal boundary layer because of the downward buoyancy forces, which oppose the upward motion established within the narrower compositional boundary layer: self-similar case with compositional and thermal layers both growing broader in upward direction. Applicable at any vertical position.

and the inner expansion of the outer solution as

$$\lim_{\eta^*\to 0} f^* = b_0 + b_1\eta^* + b_2\eta^{*2} + \ldots. \tag{32}$$

A matching of the stream function between the buoyant layers requires that

$$\lim_{\eta\to\infty} f(\eta) = R^{\frac{1}{4}} Le^{\frac{3}{4}} \lim_{\eta^*\to 0} f^*(\eta^*) \tag{33}$$

or, with both expansions written in terms of the inner variable,

$$a_0 + a_1\eta + a_2\eta^2 = (R\,Le)^{\frac{1}{2}}\left[b_0\left(\frac{Le}{R}\right)^{\frac{1}{4}} + b_1\eta + b_2\eta^2\left(\frac{R}{Le}\right)^{\frac{1}{4}}\right]. \tag{34}$$

Now, by equating like powers of η and by letting Le tend to infinity with $R\,Le$ held fixed, we obtain all of the following matching conditions:

$$b_0 = 0 \quad \to \quad f^*(0) = 0, \tag{35}$$

$$a_1 = b_1(R\,Le)^{\frac{1}{2}} \quad \to \quad f^{*\prime}(0) = \frac{f'(\infty)}{(R\,Le)^{\frac{1}{2}}}, \tag{36}$$

$$a_2 = 0 \quad \to \quad f''(\infty) = 0. \tag{37}$$

These conditions have been previously noted in (28), (29) and (23) respectively.

To construct a complete solution it is necessary to perform the following steps.

(i) Calculate the inner compositional-layer solution by solving (19)–(23). This is simply the single-diffusive solution of Kuiken; it never changes.

(ii) Calculate the outer thermal-layer solution by solving equations (25)–(29) for some chosen value of the parameter $R\,Le$ that appears in the matching condition (29).

(iii) Form the composite solution by adding the inner solution to the outer solution and subtracting the common part. In this case the common part is simply the velocity, which was matched between the layers. Example calculations are presented in figure 4 and in the solid lines on figure 2.

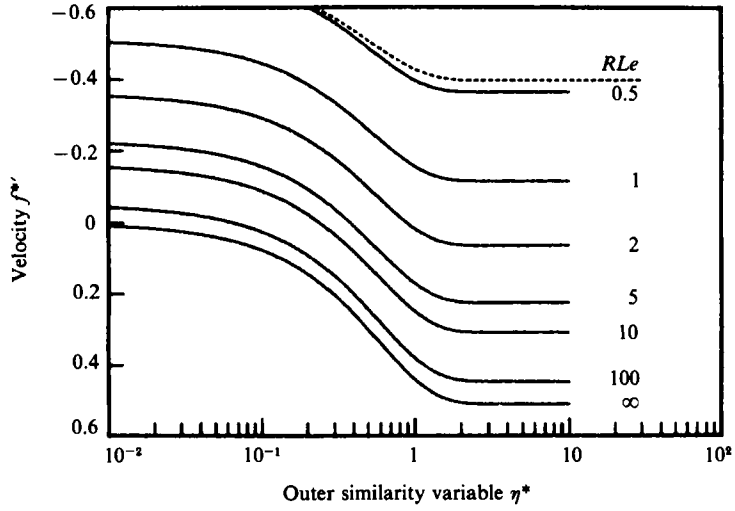

FIGURE 5. Velocity decreases in moving outward across the thermal boundary layer: non-similar case with compositional and thermal boundary layers growing broader in opposite directions. Applicable at mid-height location, $x/L = \frac{1}{2}$. Velocity $f^{*\prime}$ is positive downward, because that is the direction of motion and of boundary-layer growth in outer region.

Velocity perturbations due to thermal buoyancy are shown in figure 4. When $R\,Le$ is small the decrease in velocity within the thermal layer is relatively small compared with the dominant upward velocity that was established within the compositional layer nearer to the wall. But for larger $R\,Le$ the upward velocity is not so overwhelming, and the thermal buoyancy becomes more important. Finally, for $R\,Le = 0.66$ the upward velocity is entirely offset by the opposing thermal buoyancy.

The composite solutions, shown by solid lines in figure 2, are in good agreement with the exact numerical solutions indicated by dotted lines in that same figure. The agreement becomes even better when Le is larger, so that the approximate and exact solutions become virtually indistinguishable at $Le \approx 10^4$. But all of these solutions are self-similar, so they cannot be used to describe the counterflow regime in which the inner compositional layer is flowing upward and the outer thermal layer is flowing downward.

4. Inner-dominated counterflows

Convective boundary layers generally grow broader as they travel forward. So an upflowing compositional layer should grow broader as it rises, while a downward-flowing thermal layer should grow broader as it falls. Moreover, the boundary-layer equations are parabolic in nature, so they can only be integrated forward in the timelike streamwise direction. To do otherwise would violate the physics and would invite mathematical difficulties, such as temperature and composition that increase exponentially when the stream function is negative. Thus to describe the counterflow situation properly it is necessary to match the upflowing compositional layer to a downflowing thermal layer, such that each layer is allowed to carry information in its own direction of flow.

The inner compositional boundary layer will be treated exactly the same as in the previous analysis of similarity flows. The single-diffusive similarity solution, which

satisfies the inner equations (19)–(23), will still serve as a baseflow for the inner-dominated non-similar solutions that are now sought.

The outer thermal boundary-layer equations are almost the same as before, except that the streamwise coordinate is now x^*, which is measured downward from the top of the wall. This alteration changes the sign of the buoyancy force T in (25). Also, the velocity matching condition now reads as

$$f^{*\prime}(0) = -f'(\infty)\left(\frac{R\,Le\,x^*}{x}\right)^{-\frac{1}{2}}, \tag{38}$$

since the inner compositionally induced velocity $f'(\infty) = 0.51$ now points in the negative-x^* direction, and it varies with elevation. One might assume local similarity in the outer region, and simply solve the outer equations for different values of the parameter $R\,Le\,x^*/x$. But that would ignore some first-order corrections which arise from the variation of this parameter, and hence $f^{*\prime}(0)$, with elevation.

The non-similar character of the outer thermal region will be addressed using a local expansion technique, which is described by Sparrow, Quack & Boerner (1970), Sparrow & Yuh (1971) and Minkowycz & Sparrow (1978); it has also been recently applied to natural convection on inclined surfaces (Hassan & Eichhorn 1979; Nilson 1981). Since the equations and the symbols used there are nearly the same as here, only a brief outline of the method need be given. At the onset, it is presumed that f^* and T are each functions of two independent variables $\eta(x^*, y)$ and $\xi(x^*)$. The transport equations (1)–(4) may then be written in the following form, where $(\ )' = \partial(\ )/\partial\eta$ and $(\ )_\xi = \partial(\ )/\partial\xi$:

$$f^{*\prime\prime\prime} + T = 0, \tag{39}$$

$$T'' + 3(f^* - \xi f^*_\xi)\,T' = -3\xi f^{*\prime} T_\xi. \tag{40}$$

The corresponding boundary conditions are

$$f^*(0) = 0, \quad T(0) = 1, \quad f^{*\prime}(0) = -f'(\infty)\left(\frac{R\,Le\,x^*}{x}\right)^{-\frac{1}{2}}, \tag{41}$$

$$f^{*\prime}(\infty) = 0, \quad T(\infty) = 0. \tag{42}$$

This simple form of the equations was obtained by eliminating the inertial terms, as appropriate for large Pr, and by choosing ξ to satisfy the ordinary differential equation $4\mathrm{d}\xi/\mathrm{d}x^* = -3\xi/x^*$. The resulting non-similar transport equations (39)–(42) will be retained exactly as stated, including the derivatives with respect to the streamwise direction ξ. An additional pair of auxiliary equations, for f^*_ξ and T_ξ, must, however, be generated by differentiating the original system (39), (40) with respect to ξ. In principle, the expansion process can be extended to higher orders by successive differentiations, but the experience of others and the higher-order calculations reported in the Appendix suggest that it is generally sufficient to retain only f^*_ξ and T_ξ, and hence neglect the higher-order corrections $f^*_{\xi\xi}$ and $T_{\xi\xi}$, which would otherwise appear in the first set of auxiliary equations.

The auxiliary equations obtained by differentiation of (39), (40) may be conveniently written as follows in terms of $g = f^*_\xi$ and $h = T_\xi$:

$$g''' + h = 0, \tag{43}$$

$$h'' + 3(f^*h' + f^{*\prime}h) + 3\xi(g'h - gh') = 0. \tag{44}$$

Now, the boundary conditions for T do not vary with height, so

$$h(0, \xi) = h(\infty, \xi) = 0,$$

and $h(\eta^*)$ satisfies a homogeneous equation, so $h = 0$ is a candidate solution. Although this need not be the only solution when one of the boundaries is at infinity, it is consistent with the philosophy of the method to set the final bracket of (44) to zero to leave $h'' + 3(f^*h)' = 0$, which can be integrated once and the boundary conditions applied to demonstrate that $h = 0$ is the appropriate solution. With $h = 0$, $g''' = 0$ in (43) and hence

$$g = g(0,\xi) + g'(0,\xi)\,\eta^* + \tfrac{1}{2}g(0,\xi)\,\eta^{*2}. \tag{45}$$

The constant $g(0,\xi)$ and the quadratic coefficient $g''(0,\xi)$ must both be zero because $f^*(0,\xi) = 0$ and $f^{*\prime}(\infty,\xi) = 0$ for all values of ξ. That leaves only the linear term, which can be deduced by differentiation of the matching condition (38) with respect to x^*, noting that $\mathrm{d}x/\mathrm{d}x^* = -1$. So the final solutions of the auxiliary equations may be summarized as

$$T_\xi = 0, \tag{46}$$

$$\xi f^*_\xi = -\tfrac{2}{3}f'(\infty)\left(\frac{RLe\,x^*}{x}\right)^{-\frac{1}{2}}\left(1+\frac{x^*}{x}\right)\eta^*. \tag{47}$$

These results are now substituted back into the original zeroth-order equations (39), (40), which are then solved numerically.

Solutions of the thermal boundary-layer equations (39)–(42) are illustrated in figure 5 for various values of the parameter RLe. In all cases the vertical position is taken to be $x/L = \frac{1}{2}$, corresponding to the middle of the plate. The same curves might also be used to estimate the conditions at other vertical positions, by noting that the solutions depend mainly on the parameter $RLe\,x^*/x$, with x^*/x by itself playing a secondary role through the auxiliary non-similar adjustments. These velocity profiles apply to any value of the Lewis number, so long as it is large.

The entire range of RLe is covered by the non-similar solutions in figure 5 together with the similarity solutions in figure 4. As $RLe \to \infty$ in figure 5 the upwelling velocity $f^{*\prime}(0)$ of the compositional layer is negligible compared with the downflow velocity induced by the much stronger thermal buoyancy. In this limit the thermal boundary-layer solution becomes identical with the single-diffusive thermally driven flow, and hence $f^{*\prime}(\infty) = 0.51$ as expected. At the other end of the spectrum the non-similar solutions of figure 5 match up with the self-similar solutions from figure 4, as illustrated by comparing the similar and non-similar solutions for the particular case of $RLe = 0.5$. There is some overlap between the two families, suggesting a nearly continuous dependence on the data in transition between similar and non-similar flow regimes. However, it must be remembered that a similarity solution is the same at every elevation, in contrast with a non-similar solution, which varies rather weakly along the midsection of the plate but strongly near the ends.

It is curious that the non-similar thermal boundary layers of figure 5 can tolerate either a positive (downward) velocity or a negative (upward) velocity at the outer edge. In keeping with previously noted difficulties and our placement of blame, one might expect a failure of the mathematics if the stream function were negative at the outer edge. However, it is seen that the non-similar energy equation (40) now contains an effective stream function $F = f^* - \xi f^*_\xi$, which stays positive at large η^* in spite of the negative f^*. Were it not for the non-similar correction terms, non-similar solutions would have been unobtainable for RLe less than about two, leaving a gap in our knowledge and obscuring the non-similar/similar overlap which occurs at somewhat smaller values of RLe.

Composite solutions are illustrated in figures 6 and 7 for a midheight location of

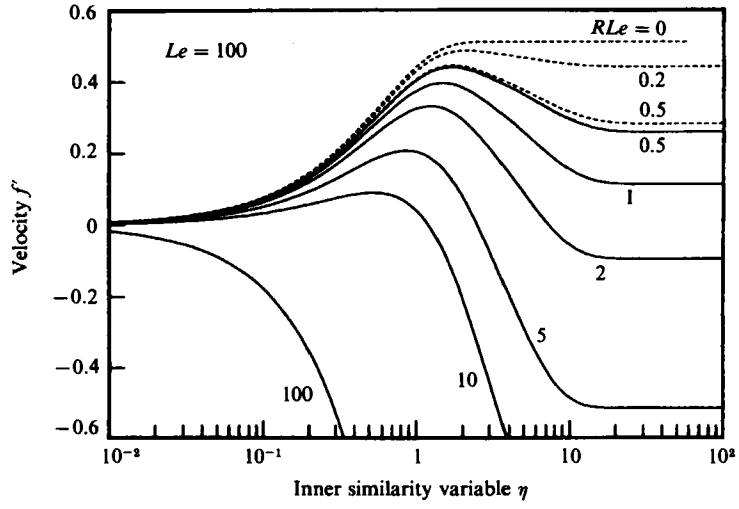

FIGURE 6. Composite velocity profiles at midheight location $x/L = \frac{1}{2}$, for non-similar inner-dominated flow. Plotted in inner variables, so that single-diffusive, compositional-only similarity solution is recovered as $R\,Le$ tends to zero.

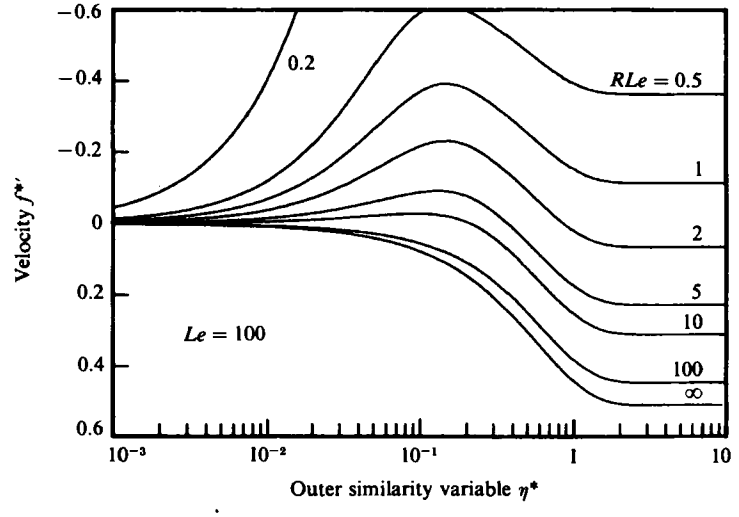

FIGURE 7. Composite velocity profiles at mid-height location $x/L = \frac{1}{2}$ for non-similar inner-dominated flow. Plotted in outer variables, so that single-diffusive, thermal-only similarity solution is recovered as $R\,Le$ tends to infinity. Velocity $f^{*\prime}$ is positive downward, as explained in figure 5 caption.

$x/L = \frac{1}{2}$, a Lewis number of 100 and various values of $R\,Le$. These velocity profiles were constructed by adding the outer thermal boundary-layer solutions of figure 5 to the inner baseflow solution of figure 2 and then subtracting the common part. The outcome depends upon the Lewis number, but only because it determines the relative scaling of the two cross-stream coordinates η and η^*. For small values of $R\,Le$ the inner buoyancy is dominant and the overall result may be viewed as a slight perturbation of the single-diffusive upflow solution, as apparent in figure 6, where the inner scaling is used to display the outcome. At intermediate values of $R\,Le$, say

five or so, the downflow is nearly as strong as the upflow. Finally, for very large values of $R\,Le$ the composite solution closely resembles a single-diffusive downflow, as best viewed in the outer scaling used in plotting figure 7. The solution curves in figures 6 and 7 are identical – it is only the scaling that has been changed to show that single diffusive results are recovered in the opposing limits when the relative buoyancy R is either very large or very small.

In presenting these results for large $R\,Le$ we tacitly violated our original premise that the flow be inner-dominated. Nevertheless, we seem to have arrived at a reasonable description of the opposite extreme. But the validity of these solutions requires some checking by comparison with similarity solutions at the outer-dominated end of the spectrum. Also, it is probably preferable to view the outer-dominated flows as perturbations of the outer, single-diffusive baseflow. These tasks will be undertaken in §§5 and 6.

5. Outer-dominated similarity solutions

The more-diffusive component, here heat, is dominant for sufficiently large values of the relative buoyancy R. In the limit as R tends to infinity the opposing compositional buoyancy is entirely absent, and the motion becomes identical with single-diffusive thermal convection. The appropriate similarity variables are then

$$\eta^* = \frac{c^* y}{x^{*\frac{1}{4}}} Pr^{\frac{1}{4}}, \quad f^* = \frac{\psi}{4\nu c^* x^{*\frac{3}{4}}} Pr^{\frac{3}{4}}, \tag{48}$$

where $c^* = (g\beta_t \Delta\theta/4\nu^2)^{\frac{1}{4}}$, and x^* is measured in the primary flow direction, which is taken to be downward for the outer-dominated case. These are the same outer variables that were used to describe the thermal boundary layer in §4.

In analogy to the inner-dominated equations (13)–(17) of §3, we now obtain the following system of ordinary differential equations:

$$f^{*'''} + T - R^{-1}C = 0, \tag{49}$$

$$T'' + 3f^*T' = 0, \tag{50}$$

$$C'' + 3\,Le\, f^*C' = 0, \tag{51}$$

with boundary conditions

$$f^*(0) = f^{*'}(0) = 0, \quad C(0) = T(0) = 1, \tag{52}$$

$$f^{*''}(\infty) = 0, \quad C(\infty) = T(\infty) = 0. \tag{53}$$

Here the inertial terms have been deleted, as appropriate for high Prandtl number, and hence the no-shear condition is applicable at the outer edge.

Numerical solutions of these double-diffusive boundary-layer equations are illustrated in figures 8 and 9 for $Le = 100$ and various values of the parameter $R\,Le^{\frac{1}{3}}$. For large R compositional buoyancy is fully suppressed and the maximum velocity is $f^{*'}(\infty) = 0.51$, in agreement with Kuiken's single-diffusive analysis. For lesser R the compositional buoyancy tends to decrease the velocity in the inner region near to the wall. For $R\,Le^{\frac{1}{3}} = 1.09$ the compositional buoyancy is just barely strong enough to reverse the flow at the wall. It is possible to calculate weakly reversed flows for slightly smaller R, but any appreciable degree of flow reversal requires a non-similar description, as described in §6. But first let us recalculate the outer-dominated similarity solutions using the method of matched asymptotic expansions.

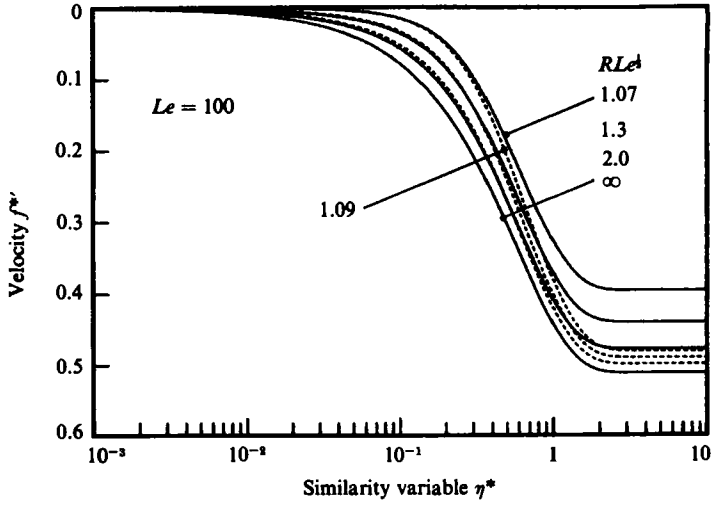

FIGURE 8. Self-similar velocity profiles for outer-dominated flow with varying strength, $RLe^{\frac{1}{2}}$ of opposing buoyancy force: comparison of matched asymptotic expansions (——) with exact numerical results (· · · · · ·). Incipient counterflow occurs at $RLe^{\frac{1}{2}} = 1.09$ and 1.07 respectively for exact and asymptotic solutions.

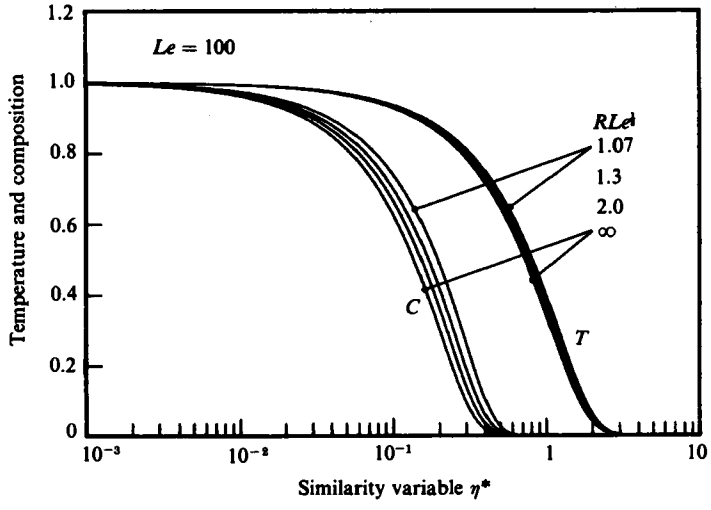

FIGURE 9. Self-similar composition and temperature profiles for outer-dominated flow: exact numerical solutions for varying strength of opposing buoyancy force. Thermal layer is much broader than compositional.

At high Lewis number the thermal boundary layer is much broader than the compositional layer, which permits an asymptotic analysis. In the outer region $C = 0$ and the complete equations (49)–(53) reduce to the form

$$f^{*'''} + T = 0, \tag{54}$$

$$T'' + 3f^*T' = 0, \tag{55}$$

$$f^{*''}(0) = f^{*'}(0) = 0, \quad T(0) = 1, \tag{56}$$

$$f^{*''}(\infty) = 0, \quad T(\infty) = 0. \tag{57}$$

The only questionable boundary condition is the vanishing velocity at the wall, since the inner buoyancy might induce an opposing motion. But here the outer solution serves as the baseflow, and the inner region remains to be adjusted. Justification for these boundary conditions derives from the inner/outer matching procedure, which is outlined in a later paragraph.

The inner compositional layer is still best described by the unstarred variables originally applied to the inner-dominated flows of earlier sections. Thus the governing equations for the inner region are written as

$$f''' - C = 0, \tag{58}$$

$$C'' + 3fC' = 0, \tag{59}$$

subject to the boundary conditions

$$f(0) = f'(0) = 0, \quad C(0) = 1, \tag{60}$$

$$C(\infty) = 0. \tag{61}$$

In keeping with self-similar rules, η and f are now based upon x^*, and the compositional buoyancy carries a negative sign, because it acts in the negative-x^* direction. As always, we neglect the thermal buoyancy in solving the inner equations, partly because R is relatively small in the counterflow situations of interest, but also because the force exerted by the thermal buoyancy within the inner layer is always very small compared with the overall thermal buoyancy force, provided only that Le is large.

Matching between the inner and outer layer provides the missing boundary condition that is needed at the outer edge of the inner layer. Proceeding as in §3, the outer expansion of the inner solution is equated to the inner expansion of the outer solution, except that this time it is most convenient to express both the expansions in terms of the outer variable η^*:

$$(R\,Le^{\frac{1}{3}})^{-\frac{3}{4}}\left[a_0\left(\frac{R}{Le}\right)^{\frac{1}{2}} + a_1\,\eta^*\left(\frac{R}{Le}\right)^{\frac{1}{4}} + a_2\,\eta^{*2}\right] = b_0 + b_1\,\eta^* + b_2\,\eta^{*2}. \tag{62}$$

If Le tends to infinity with $R\,Le^{\frac{1}{3}}$ held fixed we obtain all of the following inner/outer matching conditions:

$$b_0 = 0 \quad \rightarrow \quad f^*(0) = 0, \tag{63}$$

$$b_1 = 0 \quad \rightarrow \quad f^{*\prime}(0) = 0, \tag{64}$$

$$a_2 = (R\,Le^{\frac{1}{3}})^{\frac{3}{4}} b_2 \quad \rightarrow \quad f''(\infty) = (R\,Le^{\frac{1}{3}})^{\frac{3}{4}} f^{*\prime\prime}(0). \tag{65}$$

The first two are used in calculating the outer baseflow, which simply satisfies the usual single-diffusive equations (54)–(57). The last condition is used to calculate the inner region in which the upward compositional buoyancy is active; the effect of the outer thermal downwash is felt through the shear-stress condition $f''(\infty)$, which is applied at the outer edge of the inner layer.

The inner solution is illustrated in figure 10 for several values of the parameter $R\,Le^{\frac{1}{3}}$ that appears in the following matching condition obtained from (65):

$$\frac{\mathrm{d}^2 f}{\mathrm{d}\eta^2}(\infty) = \frac{\mathrm{d}^2 f^*}{\mathrm{d}\eta^{*2}}(0)\,(R\,Le^{\frac{1}{3}})^{\frac{3}{4}} = 0.82(R\,Le^{\frac{1}{3}})^{\frac{3}{4}}. \tag{66}$$

The numerical value of 0.82 represents the wall shear $f^{*\prime\prime}(0)$ of the outer baseflow solution. When $R\,Le^{\frac{1}{3}}$ is large the downward shear force of the outer region is much

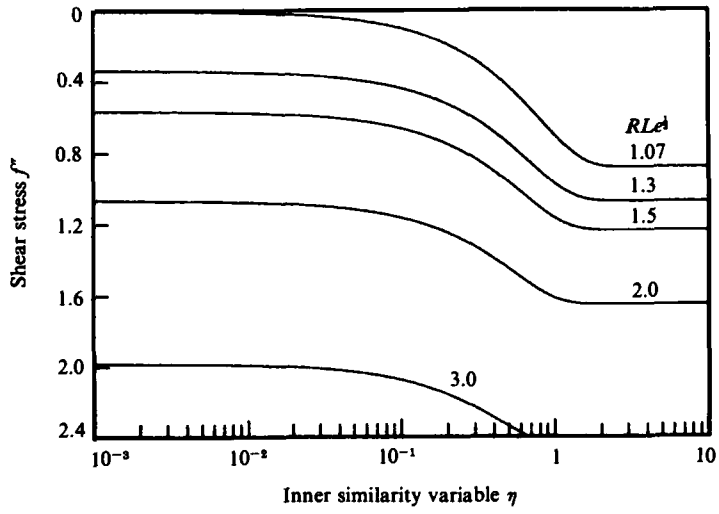

FIGURE 10. Shear stress decreases in moving inward across the compositional boundary layer because of the upward buoyancy force which opposes the downward motion established within the outer thermal layer: self-similar case with compositional and thermal layers both growing broader in the downward direction. Applicable at all heights.

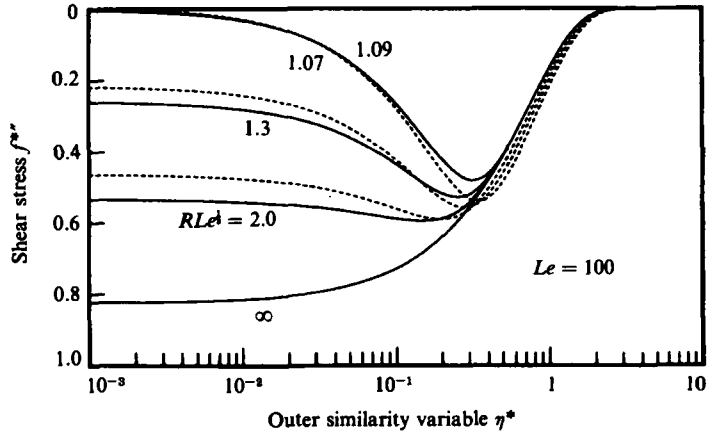

FIGURE 11. Composite shear-stress profiles (——) from asymptotic solutions compared with exact solutions (· · · · · ·): self-similar case for outer-dominated flows, same as in figures 8 and 9.

greater than the upward buoyancy force of the inner layer. Thus the shear force is nearly constant in crossing the compositional layer, as apparent in figure 10. But for smaller R the upward buoyancy becomes more significant, and for $R\,Le^{\frac{1}{3}} = 1.07$ the shear at the wall is reduced to zero, indicating a condition of incipient counterflow.

Composite profiles of the shear stress are presented in figure 11 for $Le = 100$ and various values of the parameter $R\,Le^{\frac{1}{3}}$. These profiles were constructed by adding the inner solutions of figure 10 to the outer single-diffusive baseflow and then subtracting the common part, which in this case is the shear stress, which was matched between the two layers. For large enough R the outer solution is unperturbed. At $R\,Le^{\frac{1}{3}} = 1.07$ backflow is incipient. The matched asymptotic expansions (solid lines) are in good

agreement with the exact numerical solutions (dotted lines), which were calculated from the complete equations (49)–(53).

The composite velocity profiles in figure 8 were constructed by numerical integration of the composite shear profiles just presented in figure 11. The agreement between the matched asymptotic expansions (solid lines) and the exact numerical solutions (dotted lines) is very good near the wall, but only marginal in the outer region. This is apparently because the outer velocity is an integral measure of the error committed in approximating the shear stress. Even so, the level of approximation is adequate at $Le = 100$, and agreement improves at higher Le. It is possible to reduce the discrepancy by including additional, higher-order, terms in the asymptotic expansions, but our present goal is general understanding, rather than high-level accuracy. So let us go on to apply the same first-order matching procedure to the outer-dominated portion of the counterflow regime.

6. Outer-dominated counterflows

In the non-similar counterflow regime each buoyancy layer grows broader as it advances. Since the outer layer is now dominant the baseflow solution is naturally the single-diffusive downflow induced by the thermal buoyancy acting alone. The weaker upflow zone lies close to the wall, and it must overcome the downward shear force at its outer edge.

The following inner compositional boundary-layer equations are analogous to the non-similar outer equations (39)–(42) used previously to analyse the inner-dominated counterflows:

$$f''' + C = 0, \tag{67}$$

$$C'' + 3(f - \xi f_\xi)\, C' = -3\xi f' C_\xi, \tag{68}$$

$$f(0) = f'(0) = 0, \quad C(0) = 1, \tag{69}$$

$$f''(\infty) = -f^{*\prime\prime}(0)\,(R\,Le^{\frac{1}{3}})^{\frac{3}{4}} \left(\frac{x^*}{x}\right)^{\frac{1}{4}}, \quad C(\infty) = 0. \tag{70}$$

Note that the buoyancy force now carries a positive sign, since it acts in the direction of the inner flow, and the shear force at the outer edge is now considered negative.

The non-similarity of the inner equations results from the fact that the shear stress at the outer edge varies with elevation. In analogy with the inner-dominated case, the auxiliary non-similar equations equations yield the simple analytical solutions

$$C_\xi = 0, \tag{71}$$

$$\xi f_\xi = -f^{*\prime\prime}(0)\,(R\,Le^{\frac{1}{3}})^{\frac{3}{4}} \left(\frac{x^*}{x}\right)^{\frac{1}{4}} \left(1 + \frac{x}{x^*}\right) \frac{\eta^2}{2}. \tag{72}$$

These results are substituted into the inner boundary-layer equations (67)–(70), and a numerical integration provides the final solution.

Solutions of the compositional boundary-layer equations (67)–(72) are illustrated by solid lines in figure 12 for various values of the parameter $R\,Le^{\frac{1}{3}}$. In all cases the vertical position is taken as $x^*/L = \frac{1}{2}$, corresponding to midheight. The same curves might also be used to estimate conditions at other vertical positions by noting that solutions depend mainly on $R(Le\,x^*/x)^{\frac{1}{3}}$, with x^*/x itself playing a secondary role. Also note that these inner solutions apply to any large Lewis number. It is only when the composite is constructed that a particular Le must be selected.

The entire range of $R\,Le^{\frac{1}{3}}$ is covered by the non-similar results (solid lines) together

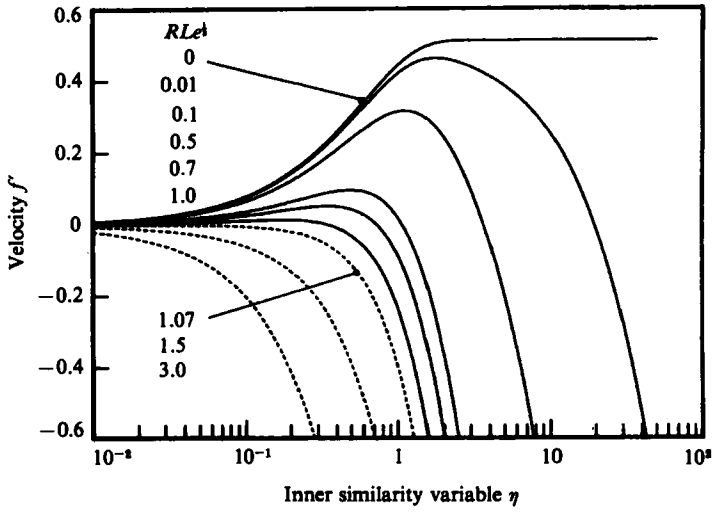

FIGURE 12. Velocity profiles in the inner region are influenced by the opposing shear force of the descending thermal layer; the parameter $R\,Le^{\frac{1}{3}}$ is a measure of this influence. Non-similar solutions (——) at mid-height $x/L = \frac{1}{2}$ agree with similarity solutions (· · · · · ·) at borderline of incipient counterflow (i.e. $R\,Le^{\frac{1}{3}} \sim 1$).

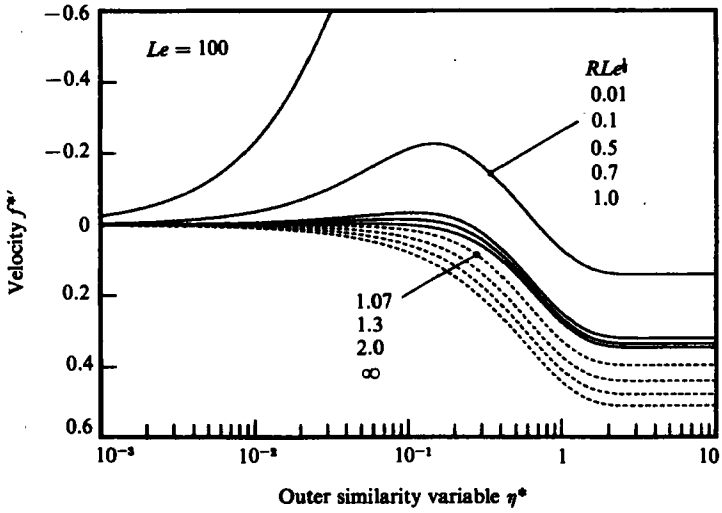

FIGURE 13. Composite velocity profiles at midheight location $x/L = \frac{1}{2}$ for non-similar outer-dominated flow. Plotted in outer variables so that single-diffusive, thermal-only similarity solution is recovered as $R\,Le^{\frac{1}{3}}$ tends to infinity. Non-similar composites (——) agree with similarity solutions (· · · · · ·) at incipient counterflow.

with the similarity solutions (dotted lines), which are all presented in figure 12. As $R\,Le^{\frac{1}{3}}$ tends to zero the downward shear force exerted by the outer thermal layer is negligible compared with the much stronger compositional buoyancy force. In this limit the compositional boundary layer becomes identical with a single-diffusive flow, and hence $f'(\infty) = 0.51$. At the opposite extreme, the non-similar solutions match up with the previous outer-dominated similarity solutions of §5, as illustrated in figure 12 by including both solutions for $R\,Le^{\frac{1}{3}}$ near unity. Thus the limiting behaviour is correct for small and large R.

Composite solutions are illustrated in figure 13 for the mid-height location $x^*/L = \frac{1}{2}$ with $Le = 100$, and various values of $R\,Le^{\frac{1}{3}}$. For large values of $R\,Le^{\frac{1}{3}}$ the outer flow overpowers the inner, and conversely for small values of the parameter. At intermediate values of $R\,Le^{\frac{1}{3}}$, say 0.2 or so, the upflow is nearly in balance with the downflow.

7. Overlap between outer-dominated and inner-dominated solutions

Two complete sets of counterflow solutions have now been derived, one called inner-dominated and the other outer-dominated. It has already been observed that each set properly matches up with its neighbouring unidirectional similarity flows. But it remains to demonstrate that some degree of overlap exists between the two sets, as one might expect to occur in the central portion of the counterflow regime. Now the opposite margins of the counterflow regime are located at $R\,Le = 0.7$ and $R\,Le^{\frac{1}{3}} = 1.0$, so let us take

$$R\,Le^{\frac{1}{2}} = 1 \tag{73}$$

as a rough indicator of the central territory where an overlap should occur. In particular, we will consider the case

$$Le = 100, \quad R = 0.1, \tag{74}$$

which complements all of the previous calculations for $Le = 100$.

The mid-height location with $x^*/x = 1$ serves as a preliminary testing ground. The inner-dominated solution of figure 7 for $R\,Le = 10$ should be the same as the outer-dominated solution of figure 13 for $R\,Le^{\frac{1}{3}} = 0.5$. Both solutions show a very weak upflow near the wall and a strong downflow with $f^{*\prime}(\infty) = 0.3$ at the outer edge. Thus the agreement is very good.

Another test of the inner-dominated/outer-dominated overlap is illustrated in figures 14 and 15, which display the non-similar velocity profiles at various distances x/L from the bottom of the plate. The only difference between these figures is that the former is plotted using inner scaling and the latter using outer scaling. In both plots, the upper elevations were calculated using inner-dominated methodology and the lower elevations using outer-dominated methodology, as indicated by the solid *vs.* dotted lines. The inner-dominated solution is nearly identical with the outer-dominated solution at $x/L = 0.7$, and the overlap extends over a considerable midsection of the plate.

The inner variables of figure 14 are most appropriate for viewing the motion near the top of the plate. The solid lines represent composite solutions obtained by the inner-dominated analysis of §4. Near the top of the plate x^*/x is small, and hence

$$R\,Le\,x^*/x < 1, \tag{75}$$

which suggests that the thermally driven downflow should not greatly perturb the upflow. Physically, the upflowing stream has run a long way and has considerable breadth at the higher elevations, so it is able to overpower the thermal downflow, which is just getting started on its downward run. It is therefore surprising to see that the thermal downflow becomes well established on the upper quarter of the plate. It must be remembered, however, that convective boundary layers grow thicker like the fourth root of distance, increasing quite rapidly near the start, but only weakly further on. The large initial growth rate of the thermal layer is felt very strongly in the non-similar corrections, which are proportional to x/x^* near the top of the plate, as seen in (70). In leaving figure 14, note that the upflow velocity persists at relatively

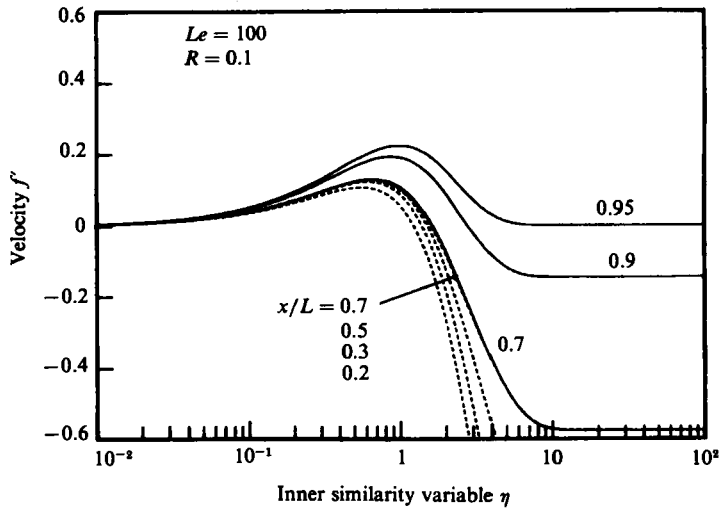

FIGURE 14. Composite velocity profiles at various elevations. Plotted in inner variables so that solution tends toward inner-dominated similarity solution at the top of the wall. Upper profiles (——) calculated from inner-dominated methodology; lower profiles (· · · · · ·) calculated from outer-dominated methodology; both solutions are identical at $x/L = 0.7$.

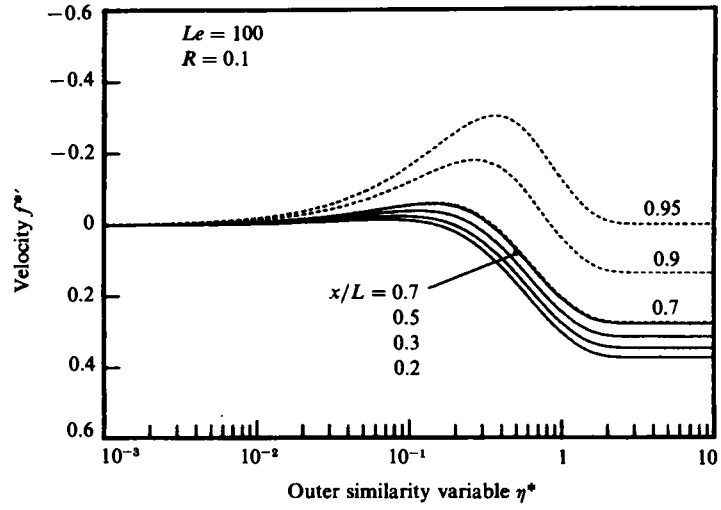

FIGURE 15. Composite velocity profiles at various elevations. Plotted in outer variables so that solutions tend toward outer-dominated similarity solution at bottom of the wall. Upper profiles (· · · · · ·) calculated from inner-dominated method; lower profiles (——) from outer-dominated method; both identical at $x/L = 0.7$.

low elevations. Even at $x/L = 0.2$, the upflow velocity is about 25% as large as it would have been in the single-diffusive case, where $f'(\infty) = 0.51$ at all elevations.

The outer variables of figure 15 are most appropriate for viewing the motion at the bottom of the plate. The solid lines represent composite solutions obtained by the outer-dominated analysis of §6, which showed the outer flow is not greatly perturbed by the inner buoyancy, provided that

$$(R\,Le^{\frac{1}{3}})^{\frac{3}{4}}\left(\frac{x^*}{x}\right)^{\frac{1}{4}} > 1. \tag{76}$$

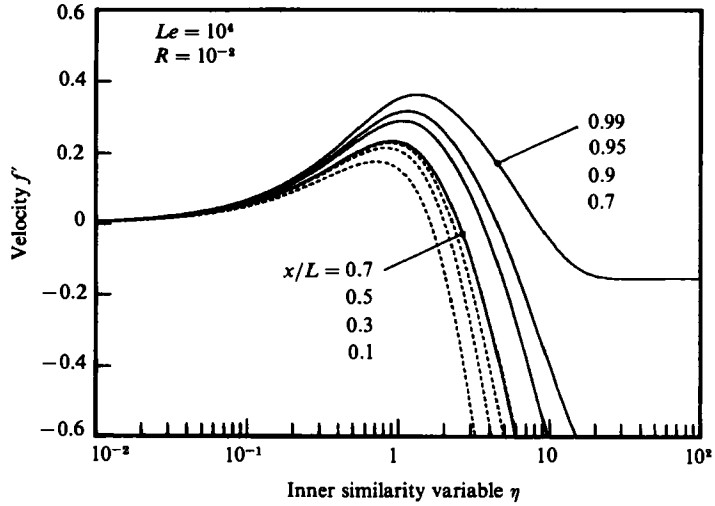

FIGURE 16. Composite velocity profiles at various elevations. Compare with figure 14. Lewis number is now much larger, but both have some value of $R\,Le^{\frac{1}{2}} = 1$, placing both in the central part of counterflow regime. Higher Lewis number tends to decouple layers.

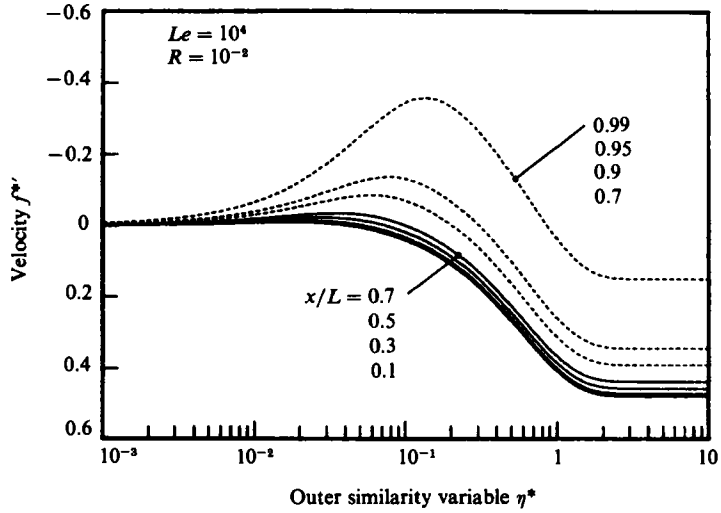

FIGURE 17. Composite velocity profiles at various elevations. Compare with figure 15; both have the same value of $R\,Le^{\frac{1}{2}} = 1$ placing both in central part of counterflow regime. Higher Lewis number tends to decouple layers, so outer and inner regions more closely resemble their respective similarity solutions.

Thus the thermal downflow should dominate near the bottom of the plate, where x^*/x becomes very large. The thermal downflow is broad and fast at the bottom of its run, so the inner layer is hardly able to rise against it. Finally note that the downflow velocity retains at least 20% of its unperturbed, single-diffusive strength ($f^{*\prime}(\infty) = 0.51$) over nearly 90% of the plate.

The influence of the Lewis number can be assessed by comparing figures 14 and 15 with 16 and 17. Both sets share the same value of $R\,Le^{\frac{1}{2}} = 1$, but the Lewis number is increased from 10^2 in 14 and 15 to 10^4 in 16 and 17. A higher Lewis number tends to increase the separation between the buoyant layers, which weakens the coupling between layers.

8. The ends of the plate

Although the flow conditions in figures 14–17 are relatively uniform along the mid-section of the plate, rapid variations are predicted to occur near the ends, particularly near the top. The validity of these near-end predictions is, however, somewhat questionable owing to a number of mathematical and physical considerations. At the upper edge of the plate the present asymptotic solutions lose their validity, since the downflowing thermal layer, presumed to begin at the top, ultimately becomes thinner than the rising compositional layer, in conflict with our matching arguments. Fortunately, this inconsistency is restricted to a very small domain (roughly, $\Delta L/L \sim R/Le$) owing to the very rapid, fourth-root growth of the thermal layer near its origin. A more serious difficulty is the presence of singularities at the upper and lower edges, where the falling and rising layers are respectively presumed to originate. Near these singularities (roughly within a few percent of the plate length) the accuracy of the non-similar solution technique becomes progressively degraded as the higher-order streamwise derivatives become larger. It is possible to remedy the situation by including additional terms in the non-similar expansion, as illustrated in the Appendix, but the effort is probably unwarranted, because the singularities are more of a mathematical annoyance than a physical reality. Laboratory observations suggest that the singularities (i.e. origins of the boundary layers) are smeared out and shifted above and below the plate owing to the recirculations occurring at the ends.

The experiments of Carey & Gebhart (1981, 1982*b*) and Sammakia & Gebhart (1983) show that some of the upward-moving fluid at the top of the plate is recirculated into the thermally driven downflow. The rising stream carries thermally differentiated fluid above the plate, causing an upward extension of the thermal boundary layer. The mathematical model, however, assumes that the thermal boundary layer begins at the top, so it should tend to underestimate the influence of the negative thermally induced buoyancy near the top.

Similarity solutions and non-similar solutions of the type considered here satisfy the partial differential equations and the cross-stream boundary conditions, wall and far-field, regardless of the origin(s) of the streamwise coordinate(s). In unidirectional boundary-layer flows there is no upstream influence, which clearly places the origin of the streamwise coordinate at the leading edge of the plate. In the present problem, however, the origin of the thermal layer lies somewhere above the top of the plate, owing to the recirculation above. Kuiken (1983) points out that an ambiguity of the origin can sometimes be resolved by enforcing an additional condition such as the location of a sink, the prescription of a temperature or velocity at a particular location, or a requirement on the global conservation of mass or energy. Barenblatt & Zeldovich (1972) likewise explain the similarity solutions are often valid only within a limited, or asymptotic, range of the timelike (here streamwise) variable and that global conservation principles can sometimes be used to remove the indeterminancy associated with the absence of initial conditions.

A shift of the upper origin provides a physically plausible and computationally simple means of assessing the influence of recirculation above the plate and accounting for it in a first-order fashion. As an upper bound, suppose that all of the rising fluid were recirculated into the downflowing layer. Conservation of mass then requires that the stream function be zero at the outer edge of the boundary layer at the top of the plate. At high Prandtl number, this implies a slight downflow in the thermal layer at the top. As Pr goes to infinity the requirement would be one of incipient counterflow at the outer edge. Examination of figures 14 and 16 shows

that this condition is met when $x/L \approx 0.95$ for $Le = 100$, and even higher for greater Le. Thus a slight upward shift of the origin should compensate for a complete recirculation of the mass. In reality, only a fraction of the upflow is recirculated. The compositionally altered fluid that drives the upflow has a relatively large buoyancy and the chemical diffusivity is relatively small, so this part of the plume should rise far above the plate. Flow reversal and recirculation should, however, be experienced by the rising fluid that has not been compositionally altered but is dragged above the plate by viscous contact with the buoyant part of the plume.

Specific features of a particular application may determine the details of the end conditions. Carey & Gebhart (1981, 1982*b*) explain that the outcome of their experiments is influenced somewhat by whether or not the vertical ice wall is partially or fully immersed in the salt-walter bath. Full immersion results in the recirculation process noted above. Partial immersion results in the accumulation of compositionally differentiated fluid at the surface, as in box-filling stratification experiments of Turner (1980) and McBirney (1980). In the intended application to magma chambers it is expected that the compositionally altered plume would rise into the stratification and that the thermally induced downflow would produce a large-scale toroidal rotation of the core, as discussed by Nilson, McBirney & Baker (1985).

Although the present analysis does not directly address the end conditions, there is considerable flexibility to satisfy the specifics of particular applications. Most importantly, it appears that the flow along the midsection of the plate is relatively insensitive to the end conditions, since only a slight shift of the coordinates is needed to compensate for full recirculation *vs.* no recirculation. The total transport of heat and mass should share that insensitivity, since they depend upon the integral of the cross-stream gradients of temperature and composition along the entire plate. These global-transport integrals might also be used to remove the indeterminacy of the upper and lower origins.

9. Summary and discussion

The overview map of figure 1 provides a reminder of the four different flow regimes considered in preceding sections.

§3. Inner-dominated similarity solutions of figure 2 served as a testing ground for the asymptotic matching of velocity between buoyancy layers.

§4. Inner-dominated counterflows are depicted in figures 6 and 7.

§5. Outer-dominated similarity solutions of figure 8 served as a testing ground for asymptotic matching of shear stress between layers.

§6. Outer-dominated counterflows are depicted in figures 12 and 13.

In the inner-dominated similarity solutions of §3 the thermal and compositional layers both grew broader in the upward direction. In the outer-dominated similarity solutions of §5 the thermal and compositional layers both grew broader in the downward direction. However, in the counterflows of §§4 and 6 each of the layers grew broader in its own direction of flow, resulting in the non-similar structures depicted in figures 14–17.

Consistency among the various classes of solutions was demonstrated in three ways:

(i) figure 6 shows that the inner-dominated similarity solutions (dotted) closely resemble their non-similar neighbours (solid) at the borderline of incipient counterflow;

(ii) figure 12 shows that the outer-dominated similarity solutions (dotted) closely resemble their non-similar neighbours (solid) at the borderline of incipient counterflow;

(iii) figures 14–17 demonstrate good overlap (dotted to solid) between the counterflow solutions obtained by inner-dominated *vs.* outer-dominated methodology.

Recall here that the similar/non similar comparisons in figures 6 and 12 were made at the mid-height location $x/L = \frac{1}{2}$ and that differences do exist near the ends of the plate. Also, it appears that, within the self-similar regions of the parameter space, non-similar solutions are also admissible. The observed continuous dependence on data would, however, suggest that the boundary lines in figure 1 do represent fairly smooth transitions between similar and non-similar behaviour.

Although many of our examples have addressed the particular case of $Le = 100$, the profiles of figures 5 and 12 do have considerable generality. Figure 5 shows the influence of upwelling compositional layer on the outer thermal downflow; the parameter $R\,Le$ is a measure of this influence. Figure 12 shows the influence of the thermal downwash on the inner compositional upflow; the parameter $R\,Le^{\frac{1}{3}}$ is a measure of this influence. Together, these two plots provide a reasonable indication of mid-height conditions within both layers for any combination of R and Le. Of course, the intermediate zone between the layers will always have some dependence on Le, but the inner and outer extremities are not greatly influenced by this whenever Le is large.

Counterflow conditions are often relatively uniform along the central portion of the plate, as apparent in figures 14–17. Near the bottom of the plate the motion becomes nearly identical with single-diffusive thermal convection. Near the top the motion tends toward single-diffusive compositional convection. These trends toward inner dominance near the top and outer dominance near the bottom are a primary non-similar feature of the bidirectional flows. The same trends were observed in the experiments of Carey & Gebhart (1982*b*) and Sammakia & Gebhart (1983).

Recirculation above the plate can be accounted for by an upward shift in the origin of the descending thermal boundary layer, in keeping with the fact that thermally differentiated fluid is dragged above the plate by viscous contact with the compositionally buoyant plume. This modification alleviates the local difficulties associated with the usual boundary-layer singularity. In comparing bounding cases of complete recirculation *vs.* none the influence was found to be localized near the top of the plate, for the parameters considered, with little impact on the global character of the flow field.

Further numerical calculations like those presented here can be easily undertaken by an interested reader. The ordinary differential equations in §§4 and 6 can be solved by a number of standard methods, using widely available general-purpose algorithms. Application to double-diffusive convection in magmas is discussed in a separate paper (Nilson *et al.* 1985), which includes the effects of viscosity variations spanning many orders of magnitude.

The focus of discussion has been the interaction between counterflowing boundary layers driven by opposing buoyancy forces. The interaction has been characterized by asymptotic matching of shear and velocity between layers. Although such an analysis is not precise, particularly in its non-similar implementation, it does provide insight into the nature of the interaction, some measures of its strength were identified ($R\,Le$ and $R\,Le^{\frac{1}{3}}$), and a simple computational procedure was demonstrated.

Appendix. Verification of non-similar solutions

The non-similar solutions presented in §§4 and 6 are computed using a two-term expansion. The first term is equivalent to a local similarity analysis. The second term takes into account the streamwise variations in stream function and temperature,

f_ξ and T_ξ, but the higher-order corrections involving $f_{\xi\xi}$, $T_{\xi\xi}$ and above have been truncated. This is not an asymptotic expansion, nor can it be formally justified in any limiting parameter range, so there is a need for *a posteriori* verification.

A number of internal checks have already been presented in the main text. Each of the two non-similar solution families, inner-dominated and outer-dominated, was found to match up reasonably well with the corresponding similarity solutions at the respective borderlines of incipient counterflow. Since that is a comparison between similar and non-similar solutions, it is not so much indicative of precision as of consistency and of reasonably smooth dependence on the physical parameters. A better indicator of accuracy is the observed overlap between the two non-similar solution families, as illustrated in the text by comparing results at midheight and slightly above. The overlap is generally quite good over the midsection ranging from $0.25 < x/L \leqslant 0.75$, with reasonable overlap often extending within 10 % of the ends. Considering the very different constructions used to generate the two families of non-similar solutions, it seems highly improbable that the observed agreement is the result of 'equivalent' errors in both solutions. Instead, the overlap should occur only in those regions where both of the two-term expansions are reasonably valid. Disagreement suggests that additional terms are needed in one of the non-similar expansions, and hence the over-extended one should be ignored.

The previous experience of others is also helpful in estimating the probable accuracy of the two-term non-similar solutions. The non-similar expansion technique used here has been previously applied to dozens of problems concerning convective motions in boundary layers. The bulk of that work was accomplished by Sparrow, Minkowycz and Eichhorn in concert with a number of other colleagues, as indicated by the sampling included in the present reference list. In most of those studies, results are reported for the first three levels of truncation (i.e. expansions including one, two or three terms). The agreement between the second and third levels has invariably been good enough to suggest that the second level is generally adequate for engineering analysis. The remainder of this Appendix presents such a comparison among the first three levels of truncation for the double-diffusive boundary-layer problem under consideration here.

The basic system of differential equations and boundary conditions for the outer, non-similar region of the inner-dominated flows is given in (39)–(42). A one-term 'local similarity' solution can be calculated by neglecting the f^*_ξ and T_ξ terms in (40) and solving directly.

The first set of auxiliary equations, generated by streamwise differentiation of (39)–(42), can be stated as follows in terms of the dependent variables $g = \xi f^*_\xi$, $G = \xi^2 f^*_{\xi\xi}$, $h = \xi T_\xi$ and $H = \xi^2 T_{\xi\xi}$:

$$g''' + h = 0, \tag{A 1}$$

$$h'' + 3(f^* - g)\,h' + 3(f^{*\prime} + g')\,h = -3(f^{*\prime} H - T' G), \tag{A 2}$$

subject to the boundary conditions

$$h(0,\xi) = h(\infty,\xi) = g(0,\xi) = g''(\infty,\xi) = 0, \tag{A 3}$$

$$g'(0,\xi) = -\tfrac{2}{3} f'(\infty)\left(Le\frac{x^*}{x}\right)^{-\frac{1}{2}}\left(1+\frac{x^*}{x}\right). \tag{A 4}$$

These differential equations are equivalent to (43)–(44), except for a slight change of notation and the retention of H and G on the right-hand side of (A 2). The two-term non-similar solutions in the text were calculated by setting H and G equal to zero

and solving (39) and (40) along with (A 1) and (A 2) for f^*, T, g and H as functions of η.

The second set of auxiliary equations, generated by streamwise differentiation of (A1) and (A2) and by dropping the third-order derivatives $f^*_{\xi\xi\xi}$ and $T_{\xi\xi\xi}$, can be stated as follows:

$$G''' + H = 0, \tag{A 5}$$

$$H'' + 3(f^* - g)H' + 6(f^{*\prime} + g')H = 3G(T' + 2h') - 3h(2g' + G'), \tag{A 6}$$

subject to the boundary conditions

$$H(0,\xi) = H(\infty,\xi) = G(0,\xi) = G''(\infty,\xi) = 0, \tag{A 7}$$

$$G'(0,\xi) = +\tfrac{2}{3}f'(\infty)\left(RLe\frac{x^*}{x}\right)^{-\frac{1}{2}}\left(\frac{1}{3} + \frac{x^*}{x} + \frac{2}{3}\left(\frac{x^*}{x}\right)^2\right). \tag{A 8}$$

Three-term nonsimilar solutions are calculated by solving the coupled equations (38), (39), (A 1), (A 2), (A 5) and (A 6) for f, T, g, h, G and H as functions of η. For simplicity of coding, these ordinary differential equations were recast into a system of 15 first-order equations, which were solved by standard shooting methods, using a Runge–Kutta integrator to march the equations and a nonlinear equation solver to adjust the 6 unknown shooting parameters. All error tolerances were set and met at 10^{-5}.

A comparison of the results obtained at the first, second and third levels of truncation is presented in figure 18 for the parameter values $RLe = 1.318$ and $x/L = \frac{1}{2}$ (i.e. $x^*/x = 1$). The corresponding values of the shooting parameters for the three-term solution are $f''(0) = 0.7236$, $T'(0) = -0.8162$, $g''(0) = -0.0492$, $h'(0) = -0.0688$, $G''(0) = -2.000$, $H'(0) = 0.2142$, with the far-field boundary conditions set at $\eta = 7.0$. The one-term solution is a poor approximation to the higher-order solutions, but the second and third levels of truncation give almost the same results. Note that this is a very severe test case, in which the upwelling velocity of the inner layer is large enough to reverse the flow completely in the outer non-similar thermal layer (see figure 5). Additional comparisons were also made at higher elevations, where convergence should be degraded, but the agreement was still acceptable at a height of $x/L = 0.9$.

A similar comparison for the inner, nonsimilar region of an outer-dominated flow is presented in figure 19, which corresponds to figure 12 of the text. The differential equations are the same as those noted previously, but the boundary conditions are derived by differentiation of (69) and (70). The physical data and shooting parameters for the third-level solution are now

$$RLe^{\frac{1}{3}} = 0.1428, \quad x/L = \tfrac{1}{2}, \quad f''(0) = 0.6193, \quad T'(0) = -0.7409, \quad g''(0) = -0.1879,$$

$$h'(0) = -0.1532, \quad G''(0) = -0.3000, \quad H'(0) = -0.0167,$$

with boundary conditions set at $\eta = 7.0$. The agreement between second and third levels is comparable to that observed in figure 18. This time, however, the one-term 'local-similarity' approximation is greatly improved. The comparison between second and third levels is nearly as good under the complete flow reversal that occurs at $RLe^{\frac{1}{3}} \approx 0.5$, but the one-term solution is no longer obtainable at that point, because the stream function is everywhere negative.

Although the first and second levels of truncation are very easily calculated by shooting or by Picard's method, the third level is considerably more difficult. In

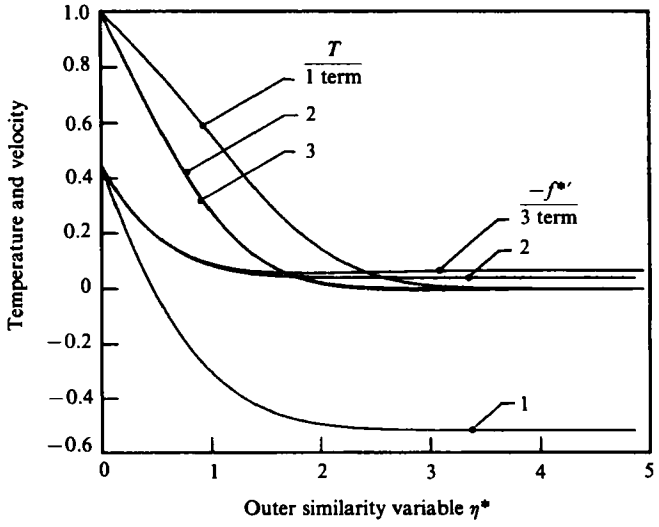

FIGURE 18. Comparison of non-similar solutions obtained at first, second and third levels of truncation for the outer region of an inner-dominated flow with $R\,Le \approx 1.3$ (see also figure 5).

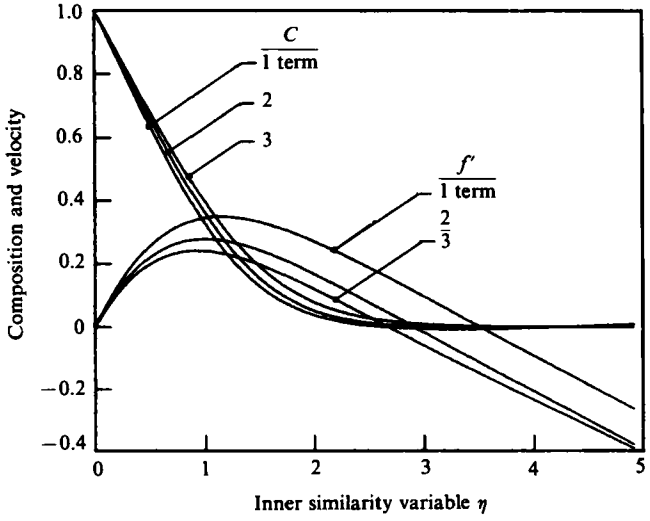

FIGURE 19. Comparison of non-similar solutions obtained at first, second and third levels of truncation for the inner region of an outer-dominated flow with $R\,Le^{\frac{1}{3}} \approx 0.14$ (see also figure 12).

shooting, it is necessary to generate a sequence of solutions for successively large choices of the interval length in order to avoid the problems associated with exponentially growing parasitic solutions. Also, there are multiple third-level solutions for given choices of the physical parameters, requiring special precautions to ensure that the root finder stays on the correct branch. Since it appears that the two families of solutions are distinguished by the sign of $G''(0)$, solutions were generated for selected values of $G''(0)$, treating the physical parameter $R\,Le$ or $R\,Le^{\frac{1}{3}}$ as one of the adjustable shooting parameters to be determined during the solution. Fortunately, the relatively good agreement between the second and third levels suggests that two terms are generally sufficient.

REFERENCES

ADAMS, J. A. & MCFADDEN, P. W. 1966 Simultaneous heat and mass transfer in free convection with opposing buoyancy forces. *AIChE J.* **6**, 584–590.

BARENBLATT, G. I. & ZELDOVICH, YA. B. 1972 Self similar solutions as intermediate asymptotics. *Ann. Rev. Fluid Mech.* **4**, 285–312.

CAREY, V. P. & GEBHART, B. 1981 Visualization of the flow adjacent to a vertical ice surface melting in cold pure water. *J. Fluid Mech.* **107**, 37–56.

CAREY, V. P. & GEBHART, B. 1982*a* Transport near a vertical ice surface melting in saline water: some numerical calculations. *J. Fluid Mech.* **117**, 379–402.

CAREY, V. P. & GEBHART, B. 1982*b* Transport near a vertical ice surface melting in saline water: experiments at low salinities. *J. Fluid Mech.* **117**, 403–424.

CEBECI, T. & STEWARTSON, K. 1983 On the calculation of separation bubbles. *J. Fluid Mech.* **133**, 287–296.

CHEN, C. F. & JOHNSON, D. H. 1984 Double Diffusive Convection: a report on an Engineering Foundation Conference. *J. Fluid Mech.* **138**, 405–416.

CHEN, C. F. & TURNER, J. S. 1980 Crystallization in a double-diffusive system. *J. Geophys. Res.* **85**, 2573–2593.

CHEN, T. S. & YUH, C. F. 1979 Combined heat and mass transfer in natural convection on an inclined plate. *Numer. Heat Transfer* **2**, 233–250.

GEBHART, B. & PERA, L. 1971 The nature of vertical natural convection resulting from combined buoyancy effects of thermal and mass diffusion. *Intl J. Heat Mass Transfer* **14**, 2025–2050.

HASSAN, M. M. & EICHHORN, R. 1979 Local nonsimilarity solutions for free convection flow and heat transfer from an inclined isothermal plate. *Trans. ASME* C: *J. Heat Transfer* **101**, 642–647.

HUPPERT, H. E. & TURNER, J. S. 1981 Double-diffusive convection. *J. Fluid Mech.* **106**, 299–329.

KLEMP, J. B. & ACRIVOS, A. 1972 A method of integrating the boundary layer equations through a region of reverse flow. *J. Fluid Mech.* **53**, 171–191.

KUIKEN, H. K. 1968 An asymptotic solution for large Prandtl number free convection. *J. Engng Maths.* **2**, 355–371.

KUIKEN, H. K. 1983 A class of backward free-convective boundary layer similarity solutions. *Intl J. Heat Mass Transfer* **26**, 655–661.

MCBIRNEY, A. R. 1980 Mixing and unmixing of magmas. *J. Volcanol. Geothermal Res.* **7**, 357–371.

MCBIRNEY, A. R. & NOYES, R. M. 1979 Crystallization and layering of the Skaergaard Intrusion. *J. Petrology* **20**, 487–554.

MINKOWYCZ, W. J. & SPARROW, E. M. 1978 Numerical solution scheme for local nonsimilarity boundary layer analysis. *Numer. Heat Transfer* **1**, 69–85.

NILSON, R. H. 1981 Natural convective boundary layer on two dimensional and axisymmetric surfaces in high Prandtl number fluids. *Trans. ASME* C: *J. Heat Transfer* **103**, 803–807.

NILSON, R. H. & BAER, M. R. 1982 Double diffusive counterbuoyant boundary layer in laminar natural convection. *Intl J. Heat Mass Transfer* **25**, 285–287.

NILSON, R. H., MCBIRNEY, A. R. & BAKER, B. H. 1985 Liquid fractionation – part II: fluid dynamics and quantitative implications for magmatic systems. *J. Volcanol. Geothermal Res.* **24**, 25–54.

OSTRACH, S. 1980 *Physico-Chem. Hydrodyn.* **1**, 233–247.

ROMERO, L. A. 1982 Nonexistence of solutions for certain double-diffusive counterbuoyant boundary layer flows. *Internal memo to A. R. Reed, Sandia Natl Labs, Albuquerque, NM* (22 October).

SAMMAKIA, B. & GEBHART, B. 1983 Transport near a vertical ice surface melting in water of various salinity levels. *Intl J. Heat Mass Transfer* **26**, 1439–1452.

SAVILLE, D. A. & CHURCHILL, S. W. 1970 Simultaneous heat and mass transfer in free convection boundary layers. *AIChE J.* **16**, 268–273.

SHAW, H. R. 1974 Diffusion of H_2O in granitic liquids. Part I: experimental data. Part II: mass transfer in magma chambers. In *Geochemical Transport and Kinetics* (ed. A. W. Hoffman, B. M. Giletti, H. S. Yoder & R. A. Yund), *Carnegie Inst. Washington Publ.* 634, pp. 139–170.

Sparrow, E. M., Quack, H. & Boerner, C. J. 1970 Local nonsimilarity boundary layer solutions. *AIAA J.* **8**, 1936–1942.

Sparrow, E. M. & Yuh, H. S. 1971 Local nonsimilarity thermal boundary layer solutions. *Trans. ASME* C: *J. Heat Transfer* **96**, 328–334.

Turner, J. S. 1974 Double-diffusive phenomena. *Ann. Rev. Fluid Mech.* **6**, 37–56.

Turner, J. S. 1980 A fluid dynamical model of differentiation and layering in magma chambers. *Nature* **285**, 213–215.

Veldman, A. E. P. 1980 On a generalized Falkner Skan equation. *J. Math. Anal. Applics* **75**, 102–111.

Walin, G. 1971 Contained non-homogeneous flow under gravity or how to stratify a fluid in the laboratory. *J. Fluid Mech.* **48**, 647–672.

Wilcox, W. R. 1961 Simultaneous heat and mass transfer in free convection. *Chem. Engng Sci.* **13**, 113–119.